Title

The relative timing of Lunar Magma Ocean solidification and the Late Heavy Bombardment inferred from highly degraded impact basin structures

Journal

Icarus, 250

ISSN

00191035

Authors

Kamata, Shunichi
Sugita, Seiji
Abe, Yutaka
et al.

Publication Date

2015-04-01

DOI

10.1016/j.icarus.2014.12.025

Peer reviewed

The relative timing of Lunar Magma Ocean solidification and the Late Heavy Bombardment inferred from highly degraded impact basin structures

Shunichi Kamata[a,b,*], Seiji Sugita[c,d], Yutaka Abe[d], Yoshiaki Ishihara[e], Yuji Harada[f], Tomokatsu Morota[g], Noriyuki Namiki[h], Takahiro Iwata[i], Hideo Hanada[j], Hiroshi Araki[h], Koji Matsumoto[j], Eiichi Tajika[c,d], Kiyoshi Kuramoto[k], Francis Nimmo[a]

[a] *Dept. Earth and Planetary Sciences, University of California, Santa Cruz, 1156 High St., Santa Cruz, CA 95064, USA*
[b] *Dept. Natural History Science, Hokkaido University, Kita-10 Nishi-8, Kita-ku, Sapporo, Hokkaido 060-0810, Japan*
[c] *Dept. Complexity Science and Engineering, The University of Tokyo, 5-1-5 Kashiwanoha, Kashiwa, Chiba 277-8561 Japan*
[d] *Dept. Earth and Planetary Science, The University of Tokyo, Bunkyo-ku, Tokyo 113-0033 Japan*
[e] *Lunar and Planetary Exploration Program Group, Japan Aerospace Exploration Agency, 3-1-1 Yoshino-dai, Chuo-ku, Sagamihara, Kanagawa 252-5210, Japan*
[f] *Planetary Science Institute, School of Earth Sciences, China University of Geosciences, 388 Lumo, Hongshan, Wuhan, Hubei 430074, China*
[g] *Graduate School of Environmental Studies, Nagoya University, Furo-cho, Chikusa-ku, Nagoya, Aichi 464-8601, Japan*
[h] *RISE Project Office, National Astronomical Observatory of Japan, 2-21-1 Osawa, Mitaka, Tokyo 181-8588, Japan*
[i] *Institute of Space and Astronautical Science, Japan Aerospace Exploration Agency, 3-1-1 Yoshino-dai, Chuo-ku, Sagamihara, Kanagawa 252-5210, Japan*
[j] *RISE Project Office, National Astronomical Observatory of Japan, 2-12 Hoshigaoka-cho, Mizusawa-ku, Oshu, Iwate 023-0861, Japan*
[k] *Dept. Cosmosciences, Hokkaido University, Kita-10 Nishi-8, Kita-ku, Sapporo, Hokkaido 060-0810, Japan*

Abstract

The solidification of the Lunar Magma Ocean (LMO) and formation of impact basins are important events that took place on the early Moon. The relative timing of these events, however, is poorly constrained. The aim of this study is to constrain the formation ages of old impact basins based on inferences of their thermal state. Most proposed basins formed before Pre-Nectarian (PN) 5 stage do not exhibit clear concentric features in either topography or gravity, suggest-

*Corresponding author
Email address: skamata@ucsc.edu (Shunichi Kamata)

ing substantial viscous lateral flow in the crust. Recent geodetic measurements reveal that the lunar crust is thinner than previously estimated, indicating that an extremely high crustal temperature is required for lateral flow to occur. In this study, we calculate lunar thermal evolution and viscoelastic deformation of basins and investigate the thermal state at the time of basin formation using recent crustal thickness models. We find that a Moho temperature >1300–1400 K at the time of basin formation is required for substantial viscous relaxation of topography to occur; the implied elastic thickness at the time of loading is <30 km. Such a high temperature can be maintained only for a short time (i.e., <50 Myr for most conditions) after solidification of the LMO or after mantle overturn if it took place; relaxed impact basins forming ≥150 Myr later than LMO solidification are unlikely. This result is in conflict with an intensive Late Heavy Bombardment (LHB) model, which assumes that most impact basins were formed at ∼3.9 Ga, since it requires LMO solidification time extremely later than previous theoretical estimates. Either the LHB was moderate, or the majority of proposed early PN basins were not in fact formed by impacts.

Keywords: Moon; Moon, interior; Impact processes; Thermal histories

1. Introduction

The very early stage of the evolution of the Moon is thought to be characterized by solidification of the Lunar Magma Ocean (LMO) and formation of large impact basins (e.g., Warren, 1985; Wilhelms, 1987; Shearer et al., 2006). The timings of these events remain poorly constrained despite of many attempts. For example, radiometric ages of lunar pristine sample rocks are varied and can be influenced by later impact heat and shock (e.g., Nemchin et al., 2009). Numerical modeling of the thermal evolution of the LMO also predicts a wide range of solidification ages; solidification of the LMO takes ∼200 Myr if a surface conductive lid develops while it takes only several tens of Myr if such a lid does not develop (e.g., Solomon & Longhi, 1977; Elkins-Tanton et al., 2011). Tidal heating on the early Moon may contribute to prolong the duration of the

LMO for ∼200–300 Myr (e.g., Meyer et al., 2010), though the tidal heating rate depends on the orbital evolution assumed.

The ages of impact basins also have large uncertainties. Based on radiometric ages of impact melts of lunar samples, the concept of a short, intense period of impacts on the Moon at ∼3.9 Ga was proposed (e.g., Tera et al., 1974; Cohen et al., 2000). This heavy bombardment on the Moon is often called the lunar cataclysm or the Late Heavy Bombardment (LHB) and has been debated for decades since it is related to the bombardment on the early Earth and the dynamical evolution of the Solar System (e.g., Stöffler et al., 2006; Gomes et al., 2005). One end-member is an intensive LHB model which assumes that most impact basins, including degraded ones, were formed during this short period (e.g., Ryder, 2002). A LHB model with a less intensive mass flux and a broader peak in time has alternatively been proposed based on a dynamical evolution model (e.g., Bottke et al., 2012; Morbidelli et al., 2012). Another hypothesis, which can explain a peak in ages of impact melts without an increase in impact flux, has also been proposed (e.g., Hartmann, 2003); the high rate of early impacts leads to pulverization of early impact melts, and only late impact melts survive. If this is the case, the formation ages of impact basins may span a long time.

The current structure of lunar impact basins reflects the thermal history since their formation. It has long been known that nearly half the impact basins identified on the Moon exhibit clear positive free-air gravity anomalies (e.g., Müller & Sjogren, 1968). Such basins are often called "mascon" basins and are thought to have large mantle uplifts (e.g., Neumann et al., 1996). Since viscosities of silicates strongly depend on temperature (e.g., Karato, 2008), mantle uplifts can relax depending on the thermal state. Recent numerical calculations (e.g., Balcerski et al., 2010; Melosh et al., 2013; Dombard et al., 2013; Freed et al., 2014) suggest that the formation of a large mantle uplift during the impact is the standard for lunar impact basins, and the main control on relaxation of mantle uplift underneath basins is not impact heating focused on the impact site but is the regional thermal state which controls subsequent long-

term viscous relaxation. Thus, highly degraded basins, which do not exhibit clear concentric features in either topography or gravity, suggest that the lunar interior was very hot when such basins formed.

The long-term thermal evolution of the Moon has also been investigated by many authors to explain various observational results, such as prolonged localized mare volcanism and a possible early core dynamo, using conductive and convective models under a wide variety of parameter conditions (e.g., Toksöz & Solomon, 1973; Stevenson et al., 1983; Konrad & Spohn, 1997; Stegman et al., 2003; Grimm, 2013; Laneuville et al., 2013). While the thermal evolution of the deep Moon depends on many factors (e.g., Evans et al., 2014), most model calculations suggest that the upper part of the Moon cooled rapidly (i.e., within several 100 Myr) unless the radiogenic heating rate was anomalously high at the base of the crust (i.e., a 10-km thick layer with >10 ppm thorium concentration) (e.g., Wieczorek & Phillips, 2000).

The goal of this study is to constrain the age of old impact basins following solidification of the LMO. If an impact basin is formed immediately after LMO solidification, the lunar interior is still very hot at the time of basin formation, and thus the initial impact structure would be highly degraded because of viscous relaxation. In contrast, if an impact basin is formed long after LMO solidification, the lunar interior is already cold at the time of basin formation, and thus the impact structure would be clearly preserved.

Viscous relaxation of impact basin topography on the Moon has also been studied for decades (e.g., Solomon et al., 1982; Mohit & Phillips, 2006; Kamata et al., 2013). Previous studies show that the observed degraded topography of an old impact basin can be reproduced well by viscous relaxation of the topography of a young impact basin, suggesting that viscous relaxation, or crustal lateral flow, is a major degradation process for lunar impact basins. The thermal structure at the time of formation of highly degraded basins, however, has not been quantitatively constrained mainly because the spatial resolution of crustal thickness models had been very low.

Recent gravity field data by Kaguya (SELENE) (e.g., Namiki et al., 2009)

and by Gravity Recovery and Interior Laboratory (GRAIL) (e.g., Zuber et al., 2013) enable us to estimate crustal thickness variations with a high spatial resolution (e.g., Ishihara et al., 2009; Wieczorek et al., 2013). Crustal thickness models based on GRAIL data and seismology further suggest that the lunar crust is thinner than previous estimates (Wieczorek et al., 2013). Since the timescale for viscous relaxation strongly depends on crustal thickness (e.g., Solomon et al., 1982; Nimmo & Stevenson, 2001), further studies of viscous relaxation on the Moon using new lunar crustal thickness models are very important for constraining the thermal state of the early Moon.

In this study, we investigate viscoelastic deformation of impact basins assuming different thermal evolution scenarios and different basin formation ages using new crustal thickness models. Section 2 shows that older impact basins have higher degrees of degradation using a recent crustal thickness model. Section 3 describes numerical calculation models employed, and Section 4 presents results obtained. Section 5 discusses implications for the LHB and some model dependencies of our work.

2. Highly degraded impact basins

The relative age of impact basins can be determined by a crater counting method; an older basin has a larger number of superposed impact craters. The relative age of basins proposed by Wilhelms (1987) has been widely used and has been broadly confirmed using recent high-resolution topography data for most impact basins (Fassett et al., 2012). This classification divides lunar geologic time into five major periods, and the first three periods cover the formation ages of the lunar impact basins: Pre-Nectarian, Nectarian, Imbrian. Pre-Nectarian (PN) is defined as a period before the formation of Nectaris, and subdivided into nine stages; PN 1 is the oldest, and PN 9 is the youngest. Nectarian is defined as a period between the formations of Nectaris and Imbrium, and subdivided into two stages. Finally, Imbrian is defined as a period after the formation of Imbrium.

Table 1 lists properties of proposed impact basins >450 km in diameter. We adopt center locations and diameters of basins determined based on Lunar Reconnaissance Orbiter (LRO) data if they are available (Head et al., 2010). Otherwise, values are taken from Wilhelms (1987). The relative age reported by Wilhelms (1987) is also summarized in Table 1. From our analysis, Grissom-White and Ingenii are excluded because the effects of crustal thinning due to South Pole-Aitken (an extremely large impact basin that covers a large portion of the southern hemisphere of the lunar farside) cannot be removed from radial profiles of these basins; crustal thickness increases with horizontal distance from the center of the South Pole-Aitken basin.

Using a GRAIL crustal thickness model (34 km on average) (Wieczorek et al., 2013), azimuthally-averaged crustal thickness profiles around these basins are created. To quantify the degree of viscous relaxation, the crustal thickness ratio, which is the minimum crustal thickness ($D_{\rm min}$) inside the basin divided by the surrounding crustal thickness ($D_{\rm cr}$) is measured for each basin. Here $D_{\rm cr}$ is defined by the thickness of the crust at 2–3 times basin radius from the basin center. Fig. 1 plots this crustal thickness ratio as a function of relative formation age.

If an impact basin is highly degraded and experienced substantial viscous relaxation (i.e., crustal lateral flow), the minimum crustal thickness approaches the surrounding crustal thickness, leading to a crustal thickness ratio $\sim$1. As shown in Fig. 1, the crustal thickness ratios for impact basins formed before the end of Pre-Nectarian (PN) 4 is $\gtrsim$0.75, suggesting that impact basins formed during PN 2–4 probably experienced substantial viscous relaxation (Ishihara et al., 2010). Changing the mean crustal thickness does not change this result.

In the following, we calculate thermal evolution and viscoelastic deformation and investigate the relation between the thermal state at the time of basin formation and the current (i.e., final) crustal thickness ratio under different parameter conditions. We note that this study assumes that early PN basins really exist. Many of the basins identified on the basis of images (Wilhelms, 1987) do not show clear concentric structures in either topography or gravity,

indicative of either significant modification or mis-identification. However, as long as some of the proposed basins really exist, our main conclusions will not be significantly affected. Conversely, the Moon may have ancient degraded basins that were not identified by Wilhelms (1987). We briefly discuss both of these issues in Section 5.

3. Model

Table 2 lists parameters adopted in our numerical calculations. We assume that the Moon consists of an anorthositic crust, peridotite mantle, and a metallic core. The crust and mantle are assumed to be Maxwell viscoelastic bodies while an inviscid fluid core is assumed. For the nominal case, the crustal and upper mantle densities are chosen to maintain consistency with a GRAIL crustal thickness model (Wieczorek et al., 2013): 2550 and 3220 kg m^{-3} for the crust and mantle, respectively. The mantle is divided into a lighter upper part and a heavier lower part because the surface gravity becomes too small if we use a density of 3220 kg m^{-3} for the entire mantle. For simplicity, we assume that a depth of 100 km is the boundary between the upper and lower mantles, and a lower mantle density of 3400 kg m^{-3} is assumed. The crustal thicknesses examined are in the range 20–60 km and each pair of thermal and relaxation calculations uses the same value. This crustal thickness is not intended to be the global mean crustal thickness, but is a value representative of the environment surrounding a particular basin. As discussed in Section 4.2, linear interpolation is applied to thermal/viscoelastic calculation results with different crustal thicknesses to determine the final topographic amplitude for each basin, where the relevant surrounding crustal thickness is listed in Table 1. These surrounding crustal thickness are determined based on a GRAIL global crustal thickness model (Wieczorek et al., 2013). When different global crustal thickness models are adopted, different density values are chosen to maintain consistency. Calculation results are not sensitive to those parameters except the crustal thickness.

In the following, we describe details of the calculations and model assump-

tions for thermal evolution and viscoelastic relaxation separately.

3.1. Thermal evolution

In order to obtain the first-order time-dependent thermal state of the upper Moon for 4.5 Gyr, the 1D thermal conduction equation,

$$\rho C_p(1+S_t)\frac{dT}{dt} = \frac{1}{r^2}\frac{d}{dr}\left(r^2 k\frac{dT}{dr}\right) + H, \tag{1}$$

is solved for the silicate parts where ρ is density, C_p is specific heat, S_t is the Stefan number, T is temperature, t is time, r is radial distance from the center of the planet, k is thermal conductivity, and H is heat production rate, respectively. We use 100 nodes with fixed spacing Δr for the crust and upper mantle and 1500 nodes for the lower mantle, respectively. The time step Δt used in our numerical model is 10^4 yr. We checked that different values for these intervals did not change our results.

The Stefan number S_t is used to take the effect of partial melting into account. When the temperature is below the solidus temperature ($T_{\rm sol}$) or above the liquidus temperature ($T_{\rm liq}$), $S_t = 0$. When $T_{\rm sol} \leq T \leq T_{\rm liq}$, on the other hand, the Stefan number S_t is given by

$$S_t = \frac{L}{C_p\left(T_{\rm liq} - T_{\rm sol}\right)} \tag{2}$$

where L is latent heat of fusion (e.g., Spohn et al., 2001). Here the melt fraction is assumed to increase linearly with temperature. S_t in the mantle is calculated using pressure-dependent solidus of peridotite (Herzberg et al., 2000), pressure-dependent liquidus of peridotite (Vlaar et al., 1994), and latent heat of fusion of basaltic magma (Fukuyama, 1985). On the other hand, $S_t = 0$ in the crust because the crustal temperatures does not exceeds 1830 K, the melting point of anorthosite (Johannes, 1978), under all calculation conditions.

For simplicity, we assume fixed temperatures at the surface (250 K) and at the core-mantle boundary (1700 K). The core-mantle boundary temperature may vary around 1600–1800 K with time (e.g., Evans et al., 2014). We found that different core-mantle boundary temperatures (i.e., 1600 and 1800 K) do not

change the temperature of the upper Moon significantly and that its effect on basin relaxation is negligible. In addition, the actual surface temperature may have been lower than our nominal value due to the "faint young sun" (e.g., Sagan & Mullen, 1972). Calculation results indicate that a surface temperature of 180 K (i.e., ∼70% of our nominal value) has little effect on the Moho temperature (much less than 100 K) and that its effect on our conclusions is negligible.

In this study, radiogenic heating due to the decay of thorium, uranium, and potassium is assumed to be the only heat source. For the nominal case, we assume a present-day thorium concentration of 1 ppm and 25 ppb in the crust and in the mantle, respectively (e.g., Jolliff et al., 2000; Warren, 2005). The concentrations of uranium and potassium are calculated using a linear relation with the thorium concentration determined based on lunar sample analyses (Korotev, 1998). We found that different radiogenic heating rates (i.e., a thorium concentration of 0.1–4.0 ppm in the crust and 150 ppb in the mantle) do not change our results significantly. Heat producing rates, decay constants, and isotopic ratios are taken from Turcotte & Schubert (2002).

Fig. 2 shows initial temperature profiles for a crustal thickness of 40 km. We use two distinctive initial temperature profiles assuming a deep LMO and a shallow LMO. For the former model, the Moho temperature of 1750 K is adopted assuming a temperature profile after mantle overturn (Elkins-Tanton et al., 2011). In this model, temperature decreases with depth and has a minimum value of 1100 K at the depth of 1000 km. Below this depth, temperature is assumed to be 1600 K. For the latter case, in contrast, the initial mantle temperature is assumed to be at the solidus of peridotite. We adopt an initial temperature of 1600 K where the solidus temperature exceeds 1600 K. In this model, temperature does not decrease with depth. These temperature profiles are similar to the initial profiles used in recent 3D lunar thermal convection models by Evans et al. (2014). For the shallow LMO case, $t = 0$ corresponds to the time of LMO solidification. For the deep LMO case, $t = 0$ corresponds to the time immediately after mantle overturn, which may occur soon after LMO solidification (Hess & Parmentier, 1995; Elkins-Tanton et al., 2011). To keep

our model settings as simple as possible, we assume an initially isothermal crust.

It is noted that our thermal evolution model is purely conductive. During early lunar evolution, the thermal state may have been controlled by solid-state mantle convection, and effective heat transport due to convection (or advection of melt) may have significantly reduced temperatures in the deep mantle (e.g., Cassen et al., 1979; Evans et al., 2014). The thermal state of the upper part of the Moon, however, would be mainly controlled by heat conduction, and basin deformation is mainly controlled by the upper viscosity structure. Consequently, our conductive model should give a good first-order approximation for the thermal state. Also, note that pure conduction is conservative in that any other effect will make cooling more rapid, and thus force basin relaxation to happen even earlier.

3.2. Viscoelastic deformation

The time-dependent temperature profiles are converted into time-dependent viscosity profiles assuming rheologies of silicates. The flow law of dry silicates is written as

$$\dot{\varepsilon} = A\sigma^n d^{-m} \exp\left(-\frac{E^*}{R_g T}\right), \tag{3}$$

$$\eta = \frac{\sigma}{2\dot{\varepsilon}}, \tag{4}$$

where $\dot{\varepsilon}$ is strain rate, A is preexponential factor, σ is stress, d is grain size, E^* is activation energy, R_g is the gas constant, η is effective viscosity, and n and m are constants, respectively (e.g., Karato, 2008). We use the rheology of dry anorthite (Rybacki & Dresen, 2000) for the crust and that of dry peridotite (Lawlis, 1998) for the mantle, respectively, both in the dislocation creep regime ($m = 0$). The rheological parameters used in this study are listed in Table 3. In order to calculate viscosity, we use stress $\sigma = 30$ MPa, which is a typical stress underneath a basin (e.g., Wieczorek & Phillips, 1999; Mohit & Phillips, 2006). For numerical reasons, we limit the viscosity to between 10^{19} Pa s and 10^{30} Pa s (e.g., Mohit & Phillips, 2006; Kamata et al., 2013). These viscosities are chosen so that the corresponding Maxwell times are much shorter and longer than

geological timescales. It is noted that a decrease in the viscosity due to partial melting is not considered. The viscosity near the solidus, however, is sufficiently low (i.e., the lower bound of 10^{19} Pa s) that its effect would not significantly affect our results. Nevertheless, the use of different rheological models may have a significant effect on viscoelastic calculation results. This issue is discussed in Section 5.2.

Our viscoelastic relaxation code is described in Kamata et al. (2012). Briefly, the spheroidal deformation of a Maxwell (i.e., linear) viscoelastic body is calculated. The governing equations are as follows (e.g., Takeuchi & Saito, 1972; Peltier, 1974):

$$\frac{d\sigma_{ji}}{dt} + \frac{\mu}{\eta}\left(\sigma_{ji} - \frac{\sigma_{kk}}{3}\delta_{ji}\right) = \left(\kappa - \frac{2\mu}{3}\right)\frac{de_{kk}}{dt}\delta_{ji} + 2\mu\frac{de_{ji}}{dt}, \quad (5)$$

$$0 = \nabla_j \cdot (\sigma_{ji} - P\delta_{ji}) + \rho\nabla_i\phi, \quad (6)$$

$$\nabla^2\phi = -4\pi G\rho, \quad (7)$$

where ∇_i is a spatial differentiation in direction of $i(= x, y, z)$, σ is stress tensor, e is strain tensor, ϕ is gravitational potential, P is hydrostatic pressure, κ is bulk modulus, μ is shear modulus, δ is the Kronecker delta, and G is the gravitational constant, respectively. A finite difference is applied to the time differentials in the constitutive equation (i.e., equation (5)), and a spherical harmonic expansion is applied to the three equations. This formulation leads to a six-component, time-dependent, inhomogeneous first-order ordinary differential equation system (Kamata et al., 2012). Then, time-marching calculations are carried out for each harmonic degree. We consider topographic loads at the surface and at the Moho of harmonic degrees up to 100; wavelengths >110 km are considered. We use 1000 nodes with fixed spacing Δr for the crust and upper mantle and 2000 nodes for the lower mantle, respectively. The time step Δt used in our numerical model is 10^{-1}–10^{5} yr depending on the time after loading. These values of interval are chosen so that the results are numerically stable and that a change in a factor of 10 does not change the results. Since these intervals are not the same as those used in the thermal evolution calculations, a linear interpolation is applied to the temperature profiles to obtain the viscosity profiles.

For simplicity, we assume that the Moon is an incompressible body, appropriate for a relatively small body. Thus the dilatation $e_{kk} = 0$ at any time; the terms with bulk modulus κ in equations (5) disappear. A shear modulus of 50 GPa is used both for the crust and mantle.

Since the start time of viscoelastic deformation is set to the basin formation age, it can be different from the start time of the thermal evolution calculation. In this study, we assumed six different basin formation times ($t_{\rm form}$): 0, 50, 100, 150, 200, and 400 Myr after the start of the thermal evolution model.

4. Results

4.1. Calculation results

Fig. 3 (a) shows typical examples of the time evolution of Moho topography for Moho loading cases. The calculation conditions other than harmonic degrees are the same. In these cases, two different deformation timescales are seen: $<10^4$ yr and 10^6–10^8 yr, depending on harmonic degree. The smaller (τ_a) and longer (τ_b) timescales correspond to those for isostatic rebound and crustal lateral flow (e.g., Solomon et al., 1982; McKenzie et al., 2000), and τ_b is the dominant timescale controlling relaxation of the Moho. The dependence of τ_b on harmonic degree (thus wavenumber) depends strongly on the boundary condition at the Moho. For long-wavelength deformation of a simple two-layer model, τ_b decreases with increasing wavenumber when the bottom layer is viscous, while τ_b is constant over different wavenumbers when the bottom layer is inviscid (McKenzie et al., 2000). The shorter deformation timescale for higher degrees that can be seen in Fig. 3 indicates that the viscosity of the mantle cannot be neglected even if it is relatively low; a model that assumes a viscous crust overlying an inviscid mantle may be too simple and would lead to qualitatively different results.

The corresponding time evolution of Moho temperature is shown in Fig. 3 (b). Since the timescale of lateral flow is shorter for higher degrees, the amplitude of high-degree Moho topography approaches zero; it relaxes completely before

cooling allows formation of a lithosphere. In contrast, the final amplitude of Moho topography approaches 0.11 for degree 10, because a lithosphere develops due to cooling and supports the load.

Fig. 4 shows the normalized amplitude of final Moho topography as a function of harmonic degree for Moho loading cases. As discussed above, a smaller final amplitude is found at higher degrees for cases with $t_{\rm form} = 50$ Myr and $D_{\rm cr} \geq 30$ km. In contrast, for the case of $t_{\rm form} = 50$ Myr and $D_{\rm cr} = 20$ km, a smaller final amplitude is found at lower degrees. This is because such a thin crust leads to a very large τ_b, and crustal lateral flow does not occur. Nevertheless, isostatic rebound with a shorter timescale τ_a still occurs. The dependence of τ_a on wavenumber is in contrast to that of τ_b; τ_a decreases with decreasing degree (e.g., Solomon et al., 1982; McKenzie et al., 2000). This dependence leads to a smaller final amplitude for lower degrees for the thin crust case.

For a given harmonic degree, a smaller final Moho topography is found for a thicker crust and a hotter initial thermal state. This is because these two factors increase the speed of lateral flow in the crust. This result is qualitatively consistent with previous studies (e.g., Zhong & Zuber, 2000; Mohit & Phillips, 2006; Kamata et al., 2013). A thicker crust and a hotter initial thermal state both lead to a higher Moho temperature at the time of loading. As we discuss in Section 4.2, the Moho temperature at the time of basin formation is the most important parameter controlling the final crustal structure.

4.2. Relaxation of early Pre-Nectarian basins

Using our viscoelastic calculation results, we calculate deformation of impact basins for ∼4.5 Gyr. For this purpose, the current crustal structures around 7 fresh impact basins are used as "initial" crustal structures. Here, the "initial" state refers to the state immediately after freezing of a melt pool and rapid deformation including the formation of the central mantle uplift (e.g., Melosh et al., 2013) but before viscous relaxation. It is also assumed that the thermal anomaly due to impact heating, including a deep melt pool formation, has already dissipated for simplicity. As discussed in Section 1, the long-term survival

of basin mantle uplift and theoretical assessments indicate that impact heating and melting focused on the impact site is unlikely to play a major role in viscous relaxation of impact basins (e.g., Balcerski et al., 2010; Melosh et al., 2013; Dombard et al., 2013; Freed et al., 2014). The ages of basins we used as the initial state are estimated to be Nectarian or Imbrian based on the superposed impact crater size-frequency distribution measurement using LRO data (Fassett et al., 2012) (see Table 1). Surface and Moho topographic undulations at the "initial" state are assumed to be loads, and final surface and Moho topographies are calculated from a linear combination of viscoelastic calculation results for surface and Moho loading cases. Given the results of our thermal/viscoelastic calculations based on different values of $D_{\rm cr}$, we then use linear interpolation to determine the final topographic amplitude for each basin, where the relevant surrounding crustal thickness is listed in Table 1. Further details of the procedure for calculating relaxed topography are given in the Appendix. As discussed below, our main conclusion is not sensitive to the choice of the initial basin shape; a high degree of degradation requires Moho temperature near the solidus.

Fig. 5 shows an example of the azimuthally-averaged initial and final (relaxed) crustal structures for Orientale, calculated assuming an initially deep LMO thermal profile and $t_{\rm form}$ = 100 Myr. Here, a GRAIL crustal thickness model with a global mean thickness of 34 km is used. The error in relaxed topography results from the error in the reference (i.e., surrounding) crustal thickness. The crustal thickness surrounding Orientale is ∼38 km, and this crustal thickness leads to a Moho temperature at $t = t_{\rm form}$ = 100 Myr of ∼1310 K. In this case, the final crustal thickness ratio is ∼0.68.

The above analysis was repeated under different conditions (i.e., initial basin shapes, initial thermal states, formation ages, and crustal thickness models) to obtain final crustal thickness ratio as a function of Moho temperature at the time of basin formation. Results are summarized in Fig. 6. This figure illustrates that Moho temperature at the time of basin formation is the primary factor controlling the final crustal thickness ratio. This result is consistent with

a previous study assuming continuously varying radial thermal and viscosity profiles (Kamata et al., 2013). The critical Moho temperature that leads to a high crustal thickness ratio (i.e., >0.75), which is similar to that observed for early PN basins, is found to be >1300–1400 K. This critical value of Moho temperature depends on the surrounding crustal thickness. We found that the critical Moho temperature is ∼1400 K when we adopt a crustal thickness model with a global mean thickness of 34 km. When we adopt another crustal thickness model with a global mean thickness of 43 km, on the other hand, the critical Moho temperature is ∼1300 K. This is again because lateral flow occurs more easily in a thicker crust (e.g., McKenzie et al., 2000)

Figure 7 shows the final crustal thickness ratio as a function of lithospheric thickness at the time of basin formation. Here, we define the lithosphere as the near-surface top layer with viscosity $\geq 10^{28}$ Pa s ($\lesssim$900 K for the crust). Because of the large activation energy of silicates, a change of the basal viscosity by a factor of 10 leads to only <10% difference in the lithospheric thickness. Our results indicate that the lithosphere needs to be initially thinner than 30 km for lateral flow to occur; otherwise a large mantle uplift could survive for billions of years. This result is in good agreement with previous elastic thickness (T_e) estimates based on analyses of admittance and coherence between topography and gravity (i.e., T_e =20–60 km for PN and Nectarian basins (Sugano & Heki, 2004) and $T_e \approx 12$ km for PN terrain (Crosby & McKenzie, 2005)).

It is noted that the early Moon could have a low-viscosity layer at the bottom of the crust if the viscosity of the uppermost mantle is higher than that of the lower crust at a given temperature. In our model, the viscosity of uppermost mantle exceeds 10^{28} Pa s while that of the lowermost crust is below 10^{28} Pa s when the Moho temperature is between ∼900 K and ∼930 K. Nevertheless, this highly viscous deep layer cannot be thick because the upper mantle temperature increases with depth and exceeds 930 K within a few km under most conditions. In addition, since this temperature range is narrow, only one layer has a viscosity $>10^{28}$ Pa s under most conditions. Thus, the appearance of a "secondary lithosphere" immediately below the Moho does not change our analysis results

significantly.

4.3. Preservation of South Pole-Aitken

Another constraint on the thermal state of the very early Moon can be obtained from the current crustal structure of the South Pole-Aitken (SPA) basin. SPA is the largest (i.e., >2000 km in diameter) and oldest (i.e., PN 1) impact basin identified on the Moon (e.g., Wilhelms, 1987). In contrast to impact basins formed during PN 2–4, SPA exhibits a clear circular topographic depression. In addition, gravity measurements over SPA suggest that SPA is almost isostatically compensated; a significant mantle uplift underneath SPA is inferred (e.g., Zuber et al., 1994; Neumann et al., 1996; Lemoine et al., 1997; Wieczorek & Phillips, 1998; Namiki et al., 2009; Ishihara et al., 2009; Wieczorek et al., 2013). These observations may be explained by the wavelength dependence of the timescale for crustal lateral flow; relaxation of longer wavelength Moho topography requires a longer time (see Section 4.1). Nevertheless, if Moho temperature at the time of SPA formation was extremely high, SPA would have relaxed.

In order to examine whether a large portion of the mantle uplift of SPA can survive when we adopt the same thermal structures which lead to high crustal thickness ratios for PN 2–4 basins, we applied the same analysis to SPA. Here, the current crustal structure around SPA was used as the initial structure. Results are shown in Fig. 8. A Moho temperature above the solidus of peridotite (i.e., ∼1400 K) at the time of SPA formation leads to a final crustal thickness ratio $\gtrsim$0.6. The conditions that lead to this final crustal thickness ratio ∼0.6 need not necessarily be rejected; a larger mantle uplift before relaxation could explain the current height.

However, the specific case with a deep LMO, a thick lunar crust (43 km on average), and $t_{\rm form}$ = 0 yr, is very unlikely. In this case, the final crustal thickness ratio ∼0.83, which is almost twice the current crustal thickness ratio. This indicates that the initial height of the mantle uplift needs to be almost twice of the current height. Because such a large initial mantle uplift would result in

a negative crustal thickness, this condition is very unlikely. As discussed below, this hottest case (if it occurred) would suggest different relative timings between LMO solidification and formation of early PN basins.

4.4. The time difference between Lunar Magma Ocean solidification and formation of early Pre-Nectarian basins

Based on the above results, the time difference between LMO solidification and formation ages of early PN basins can be estimated. As shown in Fig. 9, if the crust is thin (34 km on average), the Moho temperature can remain higher than the critical value required for substantial viscous relaxation only for the first <50 Myr. In this case, SPA does not relax even if we adopt $t_{\rm form} = 0$; the formation of early PN basins (including SPA) can overlap with the LMO. In particular, if the LMO is shallow, substantial crustal lateral flow requires basin formation prior to LMO solidification. The case with a thick crust (i.e., 43 km on average) with a shallow LMO also requires $t_{\rm form} < 50$ Myr.

The exceptional case is a thick crust with a deep LMO. This hottest Moho case requires $t_{\rm form} < 150$ Myr; much later basin formation is allowed. In addition, SPA formation needs to be later than the mantle overturn (see Section 4.3). Thus, in contrast to other cases, the formation of early PN basins is not allowed to overlap with the LMO. These constraints on the formation ages of early PN basins are summarized in Table 4.

5. Discussion

5.1. Implications for the Late Heavy Bombardment

Our results suggest that the end of PN 4 would probably have been very soon after LMO solidification (i.e., <50 Myr). Even if the lunar crust was thick and the lunar Moho was very hot immediately after mantle overturn, the time difference is <150 Myr. Because nearly half (20 out of 45) of proposed impact basins are estimated to be in or earlier than PN 4 (Wilhelms, 1987), this time difference poses a constraint on the Late Heavy Bombardment hypothesis.

First, we consider an intensive end-member LHB model. This model assumes that most impact basins, including SPA, formed during the LHB, and that PN basins formed between ∼3.9–4.0 Ga (e.g., Ryder, 2002). Consequently, this model predicts that the end of PN 4 is ∼3.9 Ga. Then, our nominal case (i.e., $t_{\rm form} < 50$ Myr) requires that LMO solidification (as well as the end of PN 4) occurred at ∼3.9 Ga. Such a late LMO solidification time is unlikely even if the LMO is thick and tidal heating is taken into account (e.g., Elkins-Tanton et al., 2011; Meyer et al., 2010). The exceptional case (i.e., a thick crust and a deep LMO) which requires $0 < t_{\rm form} < 150$ Myr does not support an intensive LHB model either. An intensive LHB model assumes that SPA formation occurred ∼4.0 Ga (e.g., Ryder, 2002), and our results then suggest LMO solidification timing needs to be $\lesssim$4.1 Ga. Again, a long time for LMO solidification is necessary. Thus, the end-member intensive LHB model is not supported by our results.

In contrast, a moderate LHB model is consistent with our results. Such a model suggests that the formation ages of SPA (PN 1) and Nectaris (N 1) are >4.3 Gyr and ∼4.1 Ga, respectively (Morbidelli et al., 2012). Consequently, the end of PN 4 soon after LMO solidification was around 4.3–4.2 Gyr. In this case, the time for LMO solidification needs to be ∼200–300 Myr, which is plausible if a surface conductive lid develops or if tidal heating is important (e.g., Solomon & Longhi, 1977; Meyer et al., 2010). The time of LMO solidification does not need to be very long (i.e., >500 Myr) even if we consider the exceptional case (i.e., $0 < t_{\rm form} < 150$ Myr). It is noted that a moderate LHB model is also supported by a recent crater-counting study using high-resolution Lunar Orbiter Laser Altimeter (LOLA) topography data. Marchi et al. (2012) reported that the size-frequency distribution near the Nectaris basin differs from that on ancient Pre-Nectarian terrains, suggesting that the LHB started around the age of Nectaris and that Pre-Nectarian basins formed prior to the LHB.

Our results are also consistent with a multiple-peak impact flux model (e.g., Tera et al., 1974). To test such a model, however, an absolute age estimation of early PN basins is necessary and is left for future studies.

It is noted that our results and a lunar impact flux model without a peak (Hartmann, 2003) do not contradict each other. In this case, early formation of impact basins (i.e., >4.2 Gyr) need not be ruled out. The end of PN 4 soon after LMO solidification would then be consistent with a plausible LMO solidification time.

Early PN basins, such as Australe and Lomonosov-Fleming, are identified as impact basins based on the distribution of mare deposits and partially preserved mountain peaks (e.g., Stuart-Alexander & Howard, 1970; Wilhelms & El-Baz, 1977; Wilhelms, 1987). However, one might argue that some of the highly degraded basins are not actual impact basins. If none of them is an impact basin, then no major basin formation occurred soon after LMO solidification; there may have been a period with a low impact flux following solidification of the LMO. The intensity during the LHB, however, is then also reduced since the total number of impact basins is smaller. Thus, this case also does not support an intensive LHB model, in which $\gtrsim$40 impact basins formed on the Moon around 3.9 Ga (Ryder, 2002).

By contrast, there may be more early PN basins than those reported by Wilhelms (1987). For example, Dirichlet-Jackson (e.g., Cook et al., 2000), not reported by Wilhelms (1987), has a large number of superposed craters, suggesting that its formation age would be very old (Fassett et al., 2012). To constrain the LHB model further, reexamination of ancient impact basin structures is very important.

Lastly, we note that our results apply strictly to basin-forming impactors. To extrapolate to the impactor flux at smaller scales, additional assumptions concerning the relevant size-frequency distribution would need to be made.

As discussed above, thin (34 km on average) and thick (43 km on average) lunar crustal thickness models lead to different relative timings of LMO solidification and the LHB. The variation in the mean crustal thickness originates from the variation in estimates of the crustal thickness at an anchor point, which is determined from a seismic data analysis (e.g., Khan et al., 2013). Consequently, future lunar missions to obtain additional seismic data will not only improve lu-

nar interior models but also provide further constraints on the evolution history of the Moon.

5.2. Model uncertainties and limitations

The timescales of viscoelastic relaxation depend strongly on the viscosity. Because the viscosity of silicates strongly depends on material and water content (e.g., Karato, 2008), it is worthwhile to discuss these effects on our conclusion.

Our rheological model assumes a dry anorthositic crust overlying a dry peridotite mantle. Recent reanalyses of Apollo samples, however, found geophysically significant amounts of water in these samples (e.g., Saal et al., 2008; Hui et al., 2013). If these samples represent a large portion of the lunar crust and mantle, the lunar interior may be rheologically wet and may be much weaker than our model. In this case, a Moho temperature much lower than the critical value obtained in this study (i.e., 1300–1400 K) would allow substantial relaxation, and a later basin formation age is allowed. Such a weak rheology, however, would not explain the existence of "mascon" basins; in order to maintain a positive free-air anomaly observed at the centers of many Nectarian and Imbrian basins, a rheological model even more viscous than our model is necessary (Melosh et al., 2013). Consequently, while some parts of the lunar interior may contain a large amount of water, a large part of the lunar upper mantle and crust is probably dry.

Laboratory experiments show that pyroxene is much more viscous than olivine and plagioclase (e.g., Mackwell et al., 1998). If the lunar lower crust is enriched in pyroxene (e.g., Wieczorek & Zuber, 2001), the actual lunar upper rheology could be much more viscous than our rheological model. If this were the case, the critical Moho temperature required for substantial crustal lateral flow would need to be much higher, and the formation ages of early PN basins would need to be earlier.

As discussed in Section 4.3, the mantle uplift of SPA would not survive if the Moho was extremely hot at the time of SPA formation (i.e., a thick crust, a deep LMO, and SPA formation $t_{\rm form} = 0$ Myr). In order to examine whether

a more viscous rheology can retain the SPA structure even under this hottest Moho condition, we conducted the same analysis on SPA using a rheology of dry Maryland diabase (∼56 vol % plagioclase, ∼43 vol % pyroxene) (Mackwell et al., 1998) for the crust. We found that SPA would still relax significantly (i.e., the final crustal thickness ratio ∼0.75) under the hottest Moho condition. This result indicates that crustal thickness and temperature are more important for relaxation than likely rheological variations; different rheologies are unlikely to change our conclusions and the above implications significantly.

Another concern is the assumption of a Newtonian (i.e., linear) rheology. The effect of nonlinearity increases as relaxation progresses; the speed of deformation under a non-Newtonian rheology becomes smaller than that under a Newtonian case (e.g., Thomas & Schubert, 1987). This is because stress decreases as relaxation progresses, resulting in a higher viscosity for a given temperature (see equations (3) and (4)). Consequently, the situation is similar to a case with a more viscous rheology. Thus, an assumption of a Newtonian rheology is conservative.

In this study, we assume conservative thermal conductivities of 1.5 and 3.0 W m^{-1} K^{-1} for the crust and mantle, respectively. If we adopt larger thermal conductivities, the Moho cools faster than our model. Consequently, substantial crustal lateral flow would require a higher Moho temperature at the time of basin formation and even earlier formation of currently degraded basins.

Furthermore, we assume a purely conductive lunar model as discussed in Section 3.1. This is also a conservative assumption; the real Moon, which would have both thermal convection and advection of melt as well as conduction, would cool faster. Thus, a higher Moho temperature and an earlier basin formation age would be needed to account for currently observed relaxed basin structures.

It is noted that we neglected near-surface yielding. Deformation of surface topography may be controlled by brittle fracture (e.g., Byerlee, 1978). Since we adopted a simple rheology (equations (3) and (4)), the viscosity of the low-temperature surface was extremely high (i.e., 10^{30} Pa s). Consequently, we underestimated the degree of surface deformation by neglecting yielding. Nev-

ertheless, the crustal thickness ratio is mainly controlled by the amplitude of undulations at the Moho (see Fig. 5), and near-surface yielding would not affect Moho deformation significantly. Thus, we regard the effect of near-surface yielding as unlikely to significantly alter our conclusions.

It is also noted that lateral variations in the interior model (i.e., heat production, temperature, density, and rheology) are not considered in this study. In the Procellarum KREEP Terrane (PKT), heat production and Moho temperature were probably much higher than those in other regions (e.g., Jolliff et al., 2000; Wieczorek & Phillips, 2000; Kamata et al., 2013; Grimm, 2013; Laneuville et al., 2013). Thus, inside the PKT, formation of degraded basins much later than LMO solidification would be allowed. Because no basin formed during the late PN inside the PKT, it is impossible to constrain the thermal state inside the PKT at that time based on our analysis; the Moho temperature could have been higher than the critical value (i.e., 1300–1400 K) during late PN. Nevertheless, it was probably lower than the critical value since the late Nectarian (see Fig. 1).

In addition, spectroscopic observations and gravity field measurements suggest that the material and density of the interior of SPA are different from those of outside SPA (e.g., Lucey et al., 1998; Nakamura et al., 2009; Besserer et al., 2014). Such large-scale lateral variations may affect relaxation of SPA. Quantification of the effect of lateral variations of mechanical properties on relaxation, however, is beyond the scope of this study and is left for future numerical studies using finite-element or finite-volume methods.

6. Conclusion

We investigated long-term viscoelastic relaxation of impact basins on the Moon under a wide variety of thermal and interior models. It is found that a critical Moho temperature >1300–1400 K at the time of basin formation is required for substantial crustal lateral flow to occur. This critical temperature corresponds to an elastic thickness $T_e < 30$ km at the time of loading, consistent

with independent estimates of Pre-Nectarian T_e values.

Proposed impact basins formed before the end of PN 4 are highly degraded so that the Moho temperature is inferred to have been higher than the critical value when these basins formed. This high critical Moho temperature suggests that the age of such basins is probably less than 50 Myr after solidification of the LMO. Even if the crust was thick and the LMO was deep enough to achieve significant heating of the Moho through mantle overturn, the age of these basins needs to be less than 150 Myr after LMO solidification. These constraints on ages of degraded basins are not consistent with an end-member LHB model in which the majority of the basins formed within a very short period at ∼3.9 Ga. Our results strongly suggest that whether or not the highly degraded early PN basins really have an impact origin may help us assess the intensity of the LHB. Whether the LMO overlapped with the LHB or not could not be determined from our analysis because of a large uncertainty in the global mean crustal thickness. A more precise crustal thickness model based on additional seismic data would therefore contribute to constraining the relative timing of the LMO and the LHB, two major events that occurred on the early Moon.

Appendix

The relaxed surface and Moho topographies of a basin are estimated in the following steps. (1) The azimuthally-averaged cross section of the present-day crustal structure within 3 times the basin main rim radius for each basin. (2) We define "a reference horizontal distance," which is 2–3 times the basin main rim radius. Surface and Moho altitudes at this reference horizontal distance are assumed to be their "unperturbed" altitudes. (3) The reference crustal thickness from these reference values are calculated. (4) Surface and Moho topographies are expanded in a spectral space using spherical harmonics. The obtained coefficients give the "initial" amplitudes of surface and Moho topographies for each harmonic degree. (5) Using the viscoelastic calculation results (i.e., ratios of initial to final amplitudes), we calculate the final surface and Moho coefficients

for each harmonic degree. Here, viscoelastic results are interpolated using the reference crustal thickness obtained at (3). (6) The final surface and Moho topographies are obtained from the superposition of spherical harmonics with final amplitudes. The above steps are repeated for different values of reference horizontal distances spanning the range 2–3, and the mean and standard deviation of recovered surface and Moho topographies are calculated. This procedure is essentially the same as that to estimate the initial crustal structure from the present-day structure using viscoelastic deformation calculations (Kamata et al., 2013).

Acknowledgments

We thank P. McGovern and an anonymous reviewer for for their careful reviews and constructive comments for improving this manuscript; M. Ohtake, Y. Karouji, S. Kobayashi, M. Hareyama, H. Nagaoka, Y. Sekine, Y. Cho, and J. Besserer for fruitful discussions; W. Bottke for his constructive comments; M. Wieczorek for making crustal thickness models available to the public. The GRAIL crustal thickness models we analyzed are available at `www.ipgp.fr/~wieczor/`. Our spherical harmonic analyses were conducted using the software archive SHTOOLS (available at `shtools.ipgp.fr`). This work was supported by JSPS Grant-in-Aid for JSPS Fellows and by KAKENHI Grant Number.

References

Balcerski, J. A., Hauck, S. A., Dombard, A. J., & Turtle, E. P. (2010). The influence of local thermal anomalies on large impact basin relaxation. *Proc. Lunar Planet. Sci. Conf. 41st*, . Abstract #2535.

Besserer, J., Nimmo, F., Wieczorek, M. A., Weber, R. C., Kiefer, W. S., McGovern, P. J., Andrews-Hanna, J. C., Smith, D. E., & Zuber, M. T. (2014). GRAIL gravity constraints on the vertical and lateral density structure of the lunar crust. *Geophys. Res. Lett.*, . doi:`10.1002/2014GL060240`.

Bottke, W. F., Vokrouhlicky, D., Minton, D., Nesvorny, D., Morbidelli, A., Brasser, R., Simonson, B., & Levison, H. F. (2012). An Archaean heavy bombardment from a destabilized extension of the asteroid belt. *Nature*, *485*, 78–81. doi:10.1038/nature10967.

Byerlee, J. (1978). Friction of rocks. *Pure Appl. Geophys.*, *116*, 615–626. doi:10.1007/BF00876528.

Cassen, P., Reynolds, R. T., Graziani, F., Summers, A., McNellis, J., & Blalock, L. (1979). Convection and lunar thermal history. *Phys. Earth Planet. Inter.*, *19*, 183–196. doi:10.1016/0031-9201(79)90082-7.

Cohen, B. A., Swindle, T. D., & Kring, D. A. (2000). Support for the lunar cataclysm hypothesis from lunar meteorite impact melt ages. *Science*, *290*, 1754–1756. doi:10.1126/science.290.5497.1754.

Cook, A. C., Watters, T. R., Robinson, M. S., Spudis, P. D., & Bussey, D. B. J. (2000). Lunar polar topography derived from Clementine stereoimages. *J. Geophys. Res.*, *105*, 12023–12033. doi:10.1029/1999JE001083.

Crosby, A., & McKenzie, D. (2005). Measurements of the elastic thickness under ancient lunar terrain. *Icarus*, *173*, 100–107. doi:10.1016/j.icarus.2004.07.017.

Dombard, A. J., Hauck, S. A., & Balcerski, J. A. (2013). On the origin of mascon basins on the Moon (and beyond). *Geophys. Res. Lett.*, *40*, 28–32. doi:10.1029/2012GL054310.

Elkins-Tanton, L. T., Burgess, S., & Yin, Q.-Z. (2011). The lunar magma ocean: Reconciling the solidification process with lunar petrology and geochronology. *Earth Planet. Sci. Lett.*, *304*, 326–336. doi:10.1016/j.epsl.2011.02.004.

Evans, A. J., Zuber, M. T., Weiss, B. P., & Tikoo, S. M. (2014). A wet, heterogeneous lunar interior: Lower mantle and core dynamo evolution. *J. Geophys. Res.*, *119*, 1061–1077. doi:10.1002/2013JE004494.

Fassett, C. I., Head, J. W., Kadish, S. J., Mazarico, E., Neumann, G. A., Smith, D. E., & Zuber, M. T. (2012). Lunar impact basins: Stratigraphy, sequence and ages from superposed impact crater populations measured from Lunar Orbiter Laser Altimeter (LOLA) data. *J. Geophys. Res.*, *117*. doi:10.1029/2011JE003951.

Freed, A. M., Johnson, B. C., Blair, D. M., Melosh, H. J., Neumann, G. A., Phillips, R. J., Solomon, S. C., Wieczorek, M. A., & Zuber, M. T. (2014). The formation of lunar mascon basins from impact to contemporary form. *J. Geophys. Res.*, . doi:10.1002/2014JE004657.

Fukuyama, H. (1985). Heat of fusion of basaltic magma. *Earth Planet. Sci. Lett.*, *73*, 407–414. doi:10.1016/0012-821X(85)90088-3.

Gomes, R., Levison, H. F., Tsiganis, K., & Morbidelli, A. (2005). Origin of the cataclysmic Late Heavy Bombardment period of the terrestrial planets. *Nature*, *435*, 466–469. doi:10.1038/nature03676.

Grimm, R. E. (2013). Geophysical constraints on the lunar Procellarum KREEP Terrane. *J. Geophys. Res.*, *118*, 768–778. doi:10.1029/2012JE004114.

Hartmann, W. K. (2003). Megaregolith evolution and cratering cataclysm models-Lunar cataclysm as a misconception (28 years later). *Meteor. Planet. Sci.*, *38*, 579–593. doi:10.1111/j.1945-5100.2003.tb00028.x.

Head, J. W., Fassett, C. I., Kadish, S. J., Smith, D. E., Zuber, M. T., Neumann, G. A., & Mazarico, E. (2010). Global distribution of large lunar craters: Implications for resurfacing and impactor populations. *Science*, *329*, 1504–1507. doi:10.1126/science.1195050.

Herzberg, C., Raterron, P., & Zhang, J. (2000). New experimental observations on the anhydrous solidus for peridotite KLB-1. *Geochem. Geophys. Geosys.*, *1*. doi:10.1029/2000GC000089.

Hess, P. C., & Parmentier, E. M. (1995). A model for the thermal and chemical evolution of the Moon's interior: Implications for the onset of mare volcanism. *Earth Planet. Sci. Lett.*, *134*, 501–514. doi:10.1016/0012-821X(95)00138-3.

Hui, H., Peslier, A. H., Zhang, Y., & Neal, C. R. (2013). Water in lunar anorthosites and evidence for a wet early Moon. *Nature Geosci.*, *6*, 177–180. doi:10.1038/ngeo1735.

Ishihara, Y., Goossens, S., Matsumoto, K., Noda, H., Araki, H., Namiki, N., Hanada, H., Iwata, T., Tazawa, S., & Sasaki, S. (2009). Crustal thickness of the Moon: Implications for farside basin structures. *Geophys. Res. Lett.*, *36*. doi:10.1029/2009GL039708.

Ishihara, Y., Morota, T., Iwata, T., Matsumoto, K., Goossens, S., & Sasaki, S. (2010). Lunar large impact basin structures and implications for thermal history. *Proc. Lunar Planet. Sci. Conf. 41st*, . Abstract #1559.

Johannes, W. (1978). Melting of plagioclase in the system Ab–An–H_2O and Qz–Ab–An–H_2O at P_{H_2O}=5 kbars, an equilibrium problem. *Contrib. Mineral. Petrol.*, *66*, 295–303. doi:10.1007/BF00373413.

Jolliff, B. L., Gillis, J. J., Haskin, L. A., Korotev, R. L., & Wieczorek, M. A. (2000). Major lunar crustal terranes: Surface expressions and crust-mantle origins. *J. Geophys. Res.*, *105*, 4197–4216. doi:10.1029/1999JE001103.

Kamata, S., Sugita, S., & Abe, Y. (2012). A new spectral calculation scheme for long-term deformation of Maxwellian planetary bodies. *J. Geophys. Res.*, *117*. doi:10.1029/2011JE003945.

Kamata, S., Sugita, S., Abe, Y., Ishihara, Y., Harada, Y., Morota, T., Namiki, N., Iwata, T., Hanada, H., Araki, H., Matsumoto, K., & Tajika, E. (2013). Viscoelastic deformation of lunar impact basins: Implications for heterogeneity in the deep crustal paleo-thermal state and radioactive element concentration. *J. Geophys. Res.*, *118*, 398–415. doi:10.1002/jgre.20056.

Karato, S. (2008). *Deformation of Earth materials: Introduction to the rheology of the solid Earth*. Cambridge: Cambridge University Press.

Khan, A., Pommier, A., Neumann, G., & Mosegaard, K. (2013). The lunar moho and the internal structure of the Moon: A geophysical perspective. *Tectonophysics*, *609*, 331–352. doi:10.1016/j.tecto.2013.02.024.

Konrad, W., & Spohn, T. (1997). Thermal history of the Moon: Implications for an early core dynamo and post-accertional magmatism. *Adv. Space Res.*, *19*, 1511–1521. doi:10.1016/S0273-1177(97)00364-5.

Korotev, R. L. (1998). Concentrations of radioactive elements in lunar materials. *J. Geophys. Res.*, *103*, 1691–1701. doi:10.1029/97JE03267.

Laneuville, M., Wieczorek, M. A., Breuer, D., & Tosi, N. (2013). Asymmetric thermal evolution of the Moon. *J. Geophys. Res.*, *118*, 1435–1452. doi:10.1002/jgre.20103.

Lawlis, J. D. (1998). *High temperature creep of synthetic olivine-enstatite aggregates*. Ph.D. thesis The Pennsylvania State University.

Lemoine, F. G. R., Smith, D. E., Zuber, M. T., Neumann, G. A., & Rowlands, D. D. (1997). A 70th degree lunar gravity model (GLGM-2) from Clementine and other tracking data. *J. Geophys. Res.*, *102*, 16339–16359. doi:10.1029/97JE01418.

Lucey, P. G., Taylor, G. J., Hawke, B. R., & Spudis, P. D. (1998). FeO and TiO_2 concentrations in the South Pole–Aitken basin: Implications for mantle composition and basin formation. *J. Geophys. Res.*, *103*, 3701–3708. doi:10.1029/97JE03146.

Mackwell, S. J., Zimmerman, M. E., & Kohlstedt, D. L. (1998). High-temperature deformation of dry diabase with application to tectonics on Venus. *J. Geophys. Res.*, *103*, 975–984. doi:10.1029/97JB02671.

Marchi, S., Bottke, W. F., Kring, D. A., & Morbidelli, A. (2012). The onset of the lunar cataclysm as recorded in its ancient crater populations. *Earth Planet. Sci. Lett.*, *325-326*, 27–38. doi:10.1016/j.epsl.2012.01.021.

McKenzie, D., Nimmo, F., Jackson, J. A., Gans, P. B., & Miller, E. L. (2000). Characteristics and consequences of flow in the lower crust. *J. Geophys. Res.*, *105*, 11029–11046. doi:10.1029/1999JB900446.

Melosh, H. J., Freed, A. M., Johnson, B. C., Blair, D. M., Andrews-Hanna, J. C., Neumann, G. A., Phillips, R. J., Smith, D. E., Solomon, S. C., Wieczorek, M. A., & Zuber, M. T. (2013). The origin of lunar mascon basins. *Science*, *340*, 1552–1555. doi:10.1126/science.1235768.

Meyer, J., Elkins-Tanton, L., & Wisdom, J. (2010). Coupled thermal–orbital evolution of the early Moon. *Icarus*, *208*, 1–10. doi:10.1016/j.icarus.2010.01.029.

Mohit, P. S., & Phillips, R. J. (2006). Viscoelastic evolution of lunar multiring basins. *J. Geophys. Res.*, *111*. doi:10.1029/2005JE002654.

Morbidelli, A., Marchi, S., Bottke, W., & Kring, D. (2012). A sawtooth-like timeline for the first billion years of lunar bombardment. *Earth Planet. Sci. Lett.*, *355-356*, 144–151. doi:10.1016/j.epsl.2012.07.037.

Müller, P. M., & Sjogren, W. L. (1968). Mascons: Lunar mass concentrations. *Science*, *161*, 680–684. doi:10.1126/science.161.3842.680.

Nakamura, R., Matsunaga, T., Ogawa, Y., Yamamoto, S., Hiroi, T., Saiki, K., Hirata, N., Arai, T., Kitazato, K., Takeda, H., Sugihara, T., Kodama, S., Ohtake, M., Haruyama, J., & Yokota, Y. (2009). Ultramafic impact melt sheet beneath the South Pole-Aitken basin on the Moon. *Geophys. Res. Lett.*, *36*. doi:10.1029/2009GL040765.

Namiki, N., Iwata, T., Matsumoto, K., Hanada, H., Noda, H., Goossens, S., Ogawa, M., Kawano, N., Asari, K., Tsuruta, S.-i., Ishihara, Y., Liu, Q.,

Kikuchi, F., Ishikawa, T., Sasaki, S., Aoshima, C., Kurosawa, K., Sugita, S., & Takano, T. (2009). Farside gravity field of the Moon from four-way Doppler measurements of SELENE (Kaguya). *Science*, *323*, 900–905. doi:10.1126/science.1168029.

Nemchin, A., Timms, N., Pidgeon, R., Geisler, T., Reddy, S., & Meyer, C. (2009). Timing of crystallization of the lunar magma ocean constrained by the oldest zircon. *Nature Geosci.*, *2*, 133–136. doi:10.1038/ngeo417.

Neumann, G. A., Zuber, M. T., Smith, D. E., & Lemoine, F. G. (1996). The lunar crust: Global structure and signature of major basins. *J. Geophys. Res.*, *101*, 16841–16863. doi:10.1029/96JE01246.

Nimmo, F., & Stevenson, D. J. (2001). Estimates of martian crustal thickness from viscous relaxation of topography. *J. Geophys. Res.*, *106*, 5085–5098. doi:10.1029/2000JE001331.

Peltier, W. R. (1974). The impulse response of a Maxwell Earth. *Rev. Geophys.*, *12*, 649–669. doi:10.1029/RG012i004p00649.

Rybacki, E., & Dresen, G. (2000). Dislocation and diffusion creep of synthetic anorthite aggregates. *J. Geophys. Res.*, *105*, 26017–26036. doi:10.1029/2000JB900223.

Ryder, G. (2002). Mass flux in the ancient Earth–Moon system and benign implications for the origin of life on Earth. *J. Geophys. Res.*, *107*. doi:10.1029/2001JE001583.

Saal, A. E., Hauri, E. H., Cascio, M. L., Van Orman, J. A., Rutherford, M. C., & Cooper, R. F. (2008). Volatile content of lunar volcanic glasses and the presence of water in the Moon's interior. *Nature*, *454*, 192–195. doi:10.1038/nature07047.

Sagan, C., & Mullen, G. (1972). Earth and Mars: Evolution of atmospheres and surface temperatures. *Science*, *177*, 52–56. doi:10.1126/science.177.4043.52.

Shearer, C. K., Hess, P. C., Wieczorek, M. A., Pritchard, M. E., Parmentier, E. M., Borg, L. E., Longhi, J., Elkins-Tanton, L. T., Neal, C. R., Antonenko, I., Canup, R. M., Halliday, A. N., Grove, T. L., Hager, B. H., Lee, D.-C., & Wiechert, U. (2006). Thermal and magmatic evolution of the Moon. *Rev. Mineral. Geochem.*, *60*, 365–518. doi:10.2138/rmg.2006.60.4.

Solomon, S. C., Comer, R. P., & Head, J. W. (1982). The evolution of impact basins: Viscous relaxation of topographic relief. *J. Geophys. Res.*, *87*, 3975–3992. doi:10.1029/JB087iB05p03975.

Solomon, S. C., & Longhi, J. (1977). Magma oceanography: 1. Thermal evolution. *Proc. Lunar Sci. Conf. 8th*, (pp. 583–599).

Spohn, T., Konrad, W., Breuer, D., & Ziethe, R. (2001). The longevity of lunar volcanism: Implications of thermal evolution calculations with 2D and 3D mantle convection models. *Icarus*, *149*, 54–65. doi:10.1006/icar.2000.6514.

Stegman, D. R., Jellinek, A. M., Zatman, S. A., Baumgardner, J. R., & Richards, M. A. (2003). An early lunar core dynamo driven by thermochemical mantle convection. *Nature*, *421*, 143–146. doi:10.1038/nature01267.

Stevenson, D. J., Spohn, T., & Schubert, G. (1983). Magnetism and thermal evolution of the terrestrial planets. *Icarus*, *54*, 466–489. doi:10.1016/0019-1035(83)90241-5.

Stöffler, D., Ryder, G., Ivanov, B. A., Artemieva, N. A., Cintala, M. J., & Grieve, R. A. F. (2006). Cratering history and lunar chronology. *Rev. Mineral. Geochem.*, *60*, 519–596. doi:10.2138/rmg.2006.60.05.

Stuart-Alexander, D. E., & Howard, K. A. (1970). Lunar maria and circular basins—a review. *Icarus*, *12*, 440–456. doi:10.1016/0019-1035(70)90013-8.

Sugano, T., & Heki, K. (2004). Isostasy of the Moon from high-resolution gravity and topography data: Implication for its thermal history. *Geophys. Res. Lett.*, *31*. doi:10.1029/2004GL022059.

Takeuchi, H., & Saito, M. (1972). Seismic surface waves. *Methods Comput. Phys.*, *11*, 217–295.

Tera, F., Papanastassiou, D., & Wasserburg, G. (1974). Isotopic evidence for a terminal lunar cataclysm. *Earth Planet. Sci. Lett.*, *22*, 1–21. doi:10.1016/0012-821X(74)90059-4.

Thomas, P. J., & Schubert, G. (1987). Finite element models of non-Newtonian crater relaxation. *J. Geophys. Res.*, *92*, E749–E758. doi:10.1029/JB092iB04p0E749.

Toksöz, M. N., & Solomon, S. C. (1973). Thermal history and evolution of the Moon. *The moon*, *7*, 251–278. doi:10.1007/BF00564634.

Turcotte, D. L., & Schubert, G. (2002). *Geodynamics, 2nd Ed.*. Cambridge: Cambridge University Press.

Vlaar, N., van Keken, P., & van den Berg, A. (1994). Cooling of the Earth in the Archaean: Consequences of pressure-release melting in a hotter mantle. *Earth Planet. Sci. Lett.*, *121*, 1–18. doi:10.1016/0012-821X(94)90028-0.

Warren, P. H. (1985). The magma ocean concept and lunar evolution. *Ann. Rev. Earth Planet. Sci.*, *13*, 201–240. doi:10.1146/annurev.ea.13.050185.001221.

Warren, P. H. (2005). "New" lunar meteorites: Implications for composition of the global lunar surface, lunar crust, and the bulk Moon. *Meteor. Planet. Sci.*, *40*, 477–506. doi:10.1111/j.1945-5100.2005.tb00395.x.

Wieczorek, M. A., Neumann, G. A., Nimmo, F., Kiefer, W. S., Taylor, G. J., Melosh, H. J., Phillips, R. J., Solomon, S. C., Andrews-Hanna, J. C., Asmar, S. W., Konopliv, A. S., Lemoine, F. G., Smith, D. E., Watkins, M. M., Williams, J. G., & Zuber, M. T. (2013). The crust of the Moon as seen by GRAIL. *Science*, *339*, 671–675. doi:10.1126/science.1231530.

Wieczorek, M. A., & Phillips, R. J. (1998). Potential anomalies on a sphere: Applications to the thickness of the lunar crust. *J. Geophys. Res.*, *103*, 1715–1724. doi:10.1029/97JE03136.

Wieczorek, M. A., & Phillips, R. J. (1999). Lunar multiring basins and the cratering process. *Icarus*, *139*, 246–259. doi:10.1006/icar.1999.6102.

Wieczorek, M. A., & Phillips, R. J. (2000). The "Procellarum KREEP Terrane": Implications for mare volcanism and lunar evolution. *J. Geophys. Res.*, *105*, 20417–20430. doi:10.1029/1999JE001092.

Wieczorek, M. A., & Zuber, M. T. (2001). The composition and origin of the lunar crust: Constraints from central peaks and crustal thickness modeling. *Geophys. Res. Lett.*, *28*, 4023–4026. doi:10.1029/2001GL012918.

Wilhelms, D. E. (1987). *The geologic history of the Moon*. U.S. Geol. Surv. Prof. Pap. 1348.

Wilhelms, D. E., & El-Baz, F. (1977). *Geologic map of the east side of the Moon*. U.S. Geol. Surv. Misc. Geol. Invest. Map., 1-948.

Zhong, S., & Zuber, M. T. (2000). Long-wavelength topographic relaxation for self-gravitating planets and implications for the time-dependent compensation of surface topography. *J. Geophys. Res.*, *105*, 4153–4164. doi:10.1029/1999JE001075.

Zuber, M. T., Smith, D. E., Lemoine, F. G., & Neumann, G. A. (1994). The shape and internal structure of the Moon from the Clementine mission. *Science*, *266*, 1839–1843. doi:10.1126/science.266.5192.1839.

Zuber, M. T., Smith, D. E., Watkins, M. M., Asmar, S. W., Konopliv, A. S., Lemoine, F. G., Melosh, H. J., Neumann, G. A., Phillips, R. J., Solomon, S. C., Wieczorek, M. A., Williams, J. G., Goossens, S. J., Kruizinga, G., Mazarico, E., Park, R. S., & Yuan, D.-N. (2013). Gravity field of the Moon from the Gravity Recovery and Interior Laboratory (GRAIL) mission. *Science*, *339*, 668–671. doi:10.1126/science.1231507.

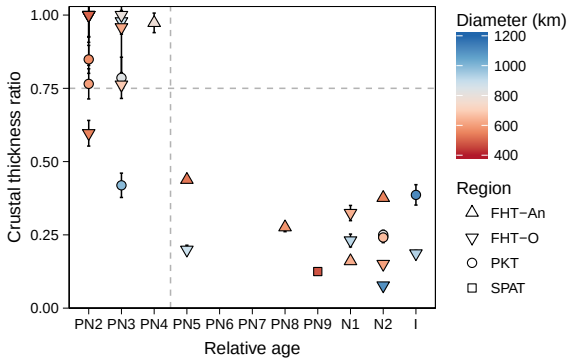

Figure 1: Crustal thickness ratio as a function of relative formation age for impact basins larger than 450 km in diameter. The crustal thickness ratio is defined as the minimum crustal thickness divided by the surrounding crustal thickness. A GRAIL crustal thickness model (34 km on average) and relative age data from Wilhelms (1987) are adopted. Regional geological unit names from Jolliff et al. (2000) are shown. Most impact basins formed before Pre-Nectarian 5 have crustal thickness ratios $\sim$1, suggesting substantial lateral flow in the crust.

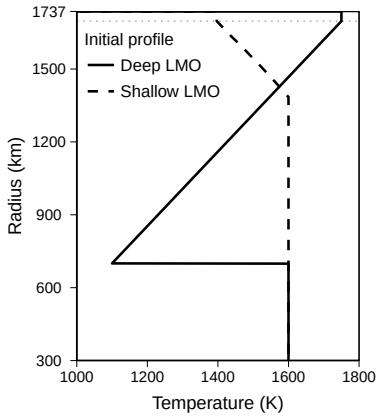

Figure 2: Initial temperature profiles for crustal thickness $D_{\rm cr} = 40$ km. The horizontal gray dashed line indicates the depth of Moho. The deep LMO case assumes an inverted thermal state caused by mantle overturn (Elkins-Tanton et al., 2011).

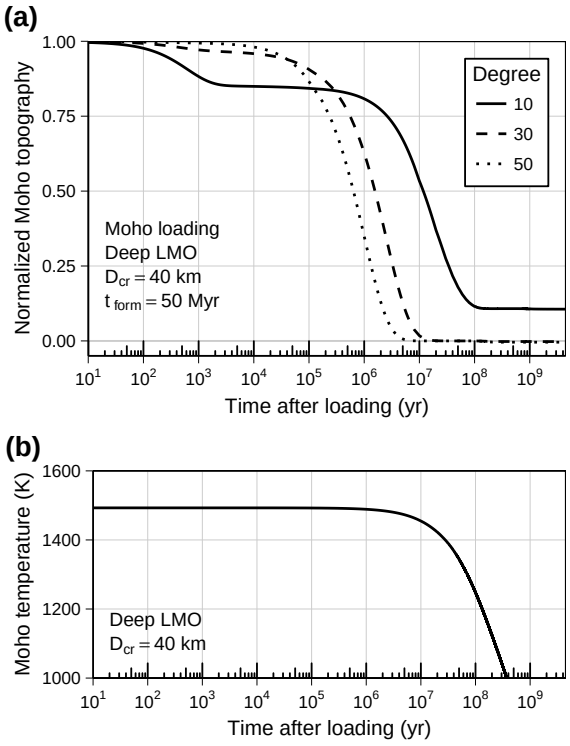

Figure 3: Time evolution of (a) Moho topography for Moho loading cases and (b) Moho temperature. (a) Results for harmonic degrees 10, 30, and 50 are illustrated. Other calculation conditions are shown. High-degree (short-wavelength) Moho topography completely relaxes before Moho cools.

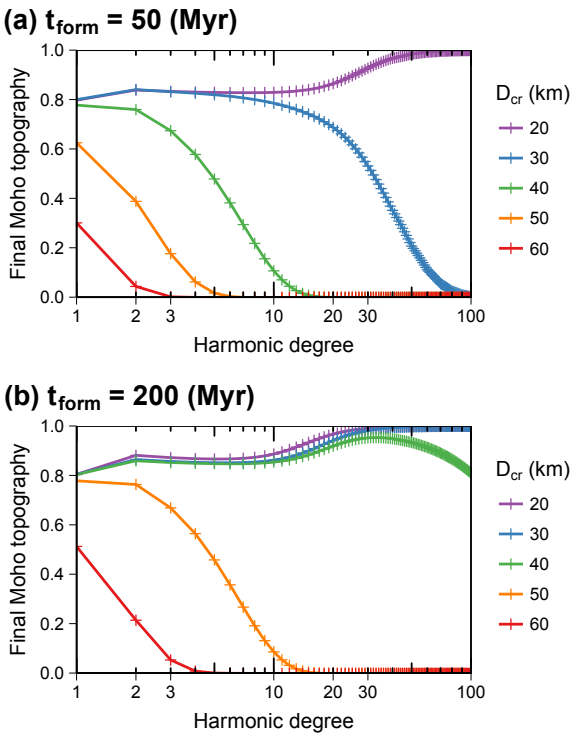

Figure 4: Final amplitude of topographic undulation at the Moho for Moho loading cases. A deep LMO thermal state is assumed. (a) and (b) show results for $t_{\rm form}$ = 50 Myr and $t_{\rm form}$ = 200 Myr, respectively. The final Moho topographic amplitude depends strongly on crustal thickness, formation age, and harmonic degree.

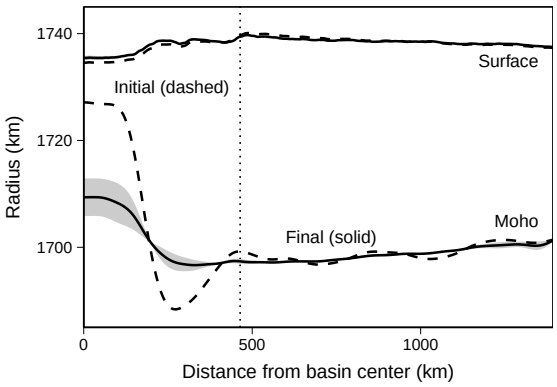

Figure 5: Azimuthally-averaged initial and final (relaxed) crustal structures around Orientale for a deep LMO case and $t_{\rm form} = 100$ Myr. The vertical dotted line indicates the basin main rim distance. A GRAIL crustal thickness model (34 km on average) is used. The crustal thickness ratios for the initial and final states are 0.20 ± 0.01 and 0.68 ± 0.08, respectively.

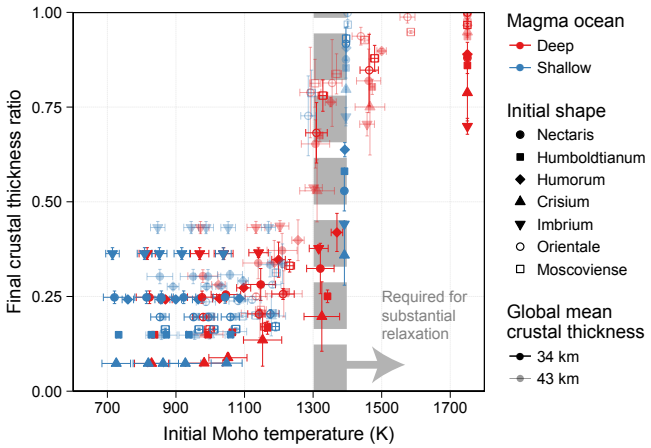

Figure 6: Final crustal thickness ratio as a function of initial Moho temperature. Results under all calculation conditions are shown. For most cases, a Moho temperature >1300–1400 K at the time of basin formation is necessary to achieve a large (i.e., ∼0.75) final crustal thickness ratio, which is similar to that observed for impact basins formed before Pre-Nectarian 5 (Fig. 1).

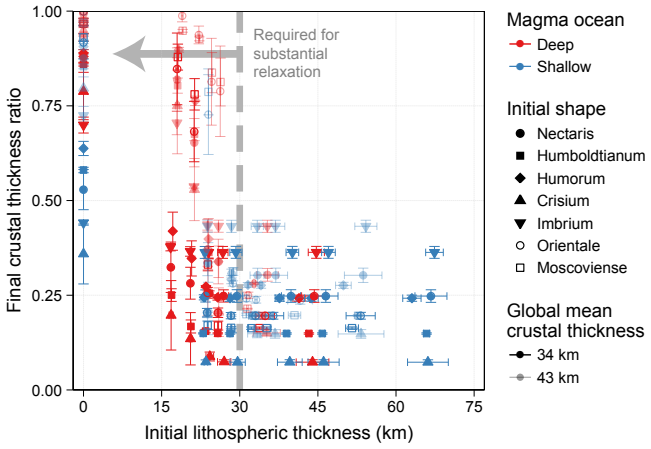

Figure 7: Final crustal thickness ratio as a function of initial lithospheric thickness. A basal viscosity of the lithosphere of 10^{28} Pa s is adopted. Results under all calculation conditions are shown. A lithospheric thickness < 30 km at the time of basin formation is necessary for lateral flow to occur.

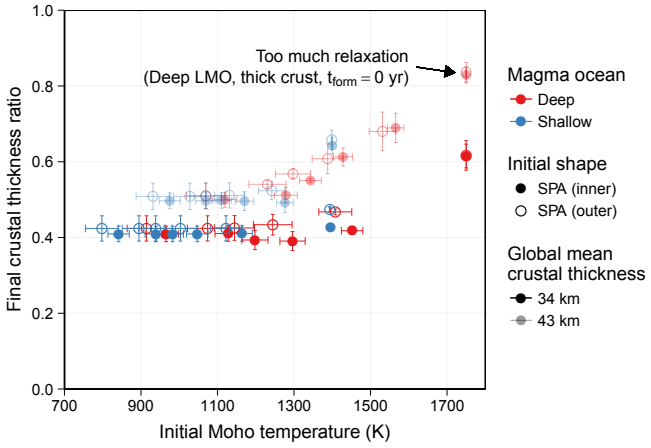

Figure 8: Final crustal thickness ratio as a function of initial Moho temperature for South Pole-Aitken (SPA). The cases of a deep LMO, a thick crust, and $t_{\rm form} = 0$ yr lead to a final crustal thickness ratio >0.8, indicating that SPA would relax significantly.

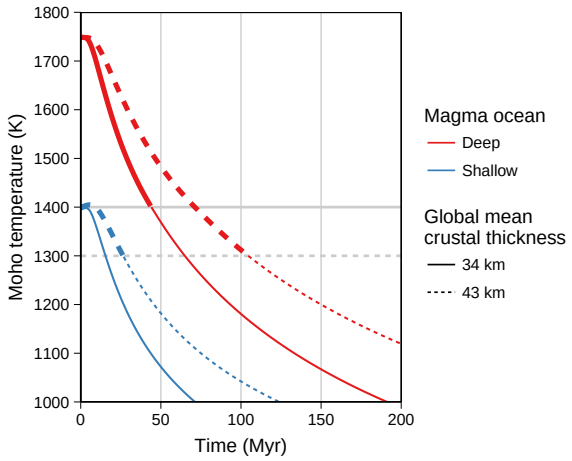

Figure 9: The time evolution of Moho temperature. Results for crustal thicknesses 34 km and 43 km are shown. The gray solid and dashed horizontal lines indicate the lowest temperature required for substantial relaxation for thinner and thicker crust models, respectively. The thick parts of curves indicates formation ages allowed for early Pre-Nectarian basins. The 43 km-thick crust with a deep LMO can allow substantial viscous relaxation for <150 Myr. Other cases allow substantial viscous relaxation only for <50 Myr.

Table 1: Properties of impact basins analyzed in this study.

Name	Center	Diameter (km)	Age[1b]	Region[2]	Surrounding crustal thickness (km)[3]	Crustal thickness ratio[3]
South Pole-Aitken (inner)[a]	170°W, 54°S	2050	PN1 (PN)	SPAT	37.5 ± 1.7	0.41 ± 0.02
South Pole-Aitken (outer)[b]	180°E, 56°S	2500	PN1 (PN)	SPAT	34.4 ± 2.3	0.43 ± 0.03
Werner-Airy[b]	12°E, 24°S	500	PN2	FHT-O	30.3 ± 1.6	1.00 ± 0.05
Balmer-Kapteyn[b]	69°E, 15.5°S	550	PN2	FHT-O	29.3 ± 0.5	0.61 ± 0.01
Flamsteed-Billy[b]	45°W, 7.5°S	570	PN2	PKT	29.9 ± 1.7	0.79 ± 0.05
Marginis[b]	84°E, 20°N	580	PN2	FHT-O	28.7 ± 1.0	1.00 ± 0.03
Al-Khwarizmi-King[b]	112°E, 1°N	590	PN2	FHT-O	34.9 ± 0.7	1.00 ± 0.02
Insularum[b]	18°W, 9°N	600	PN2	PKT	27.1 ± 0.3	0.79 ± 0.01
Tsiolkovsky-Stark[b]	128°E, 15°S	700	PN2	FHT-O	36.4 ± 0.9	1.00 ± 0.03
Lomonosov-Fleming[b]	105°E, 19°N	620	PN3	FHT-O	33.9 ± 0.5	0.95 ± 0.01
Mutus-Vlacq[b]	21°E, 51.5°S	690	PN3	FHT-O	33.7 ± 1.2	0.78 ± 0.03
Tranquillitatis[b]	40°E, 7°N	800	PN3	FHT-O	31.0 ± 0.9	0.95 ± 0.03
Nubium[a]	15.4°W, 18.6°S	835	PN3 (PN)	PKT	32.1 ± 0.6	0.75 ± 0.01
Australe[b]	94.5°E, 51.5°S	880	PN3	FHT-O	31.6 ± 0.6	0.98 ± 0.02
Fecunditatis[b]	52°E, 4°S	990	PN3	PKT	30.3 ± 0.6	0.42 ± 0.01
Keeler-Heaviside[b]	162°E, 10°S	780	PN4	FHT-An	38.1 ± 0.6	0.98 ± 0.02
Coulomb-Sarton[b]	123°W, 52°N	530	PN5 (PN)	FHT-An	40.4 ± 0.5	0.44 ± 0.01
Smythii[a]	86.6°E, 1.83°S	887	PN5 (PN)	FHT-O	31.9 ± 1.1	0.20 ± 0.01

Table 1: Properties of impact basins analyzed in this study (continue).

Name	Center	Diameter (km)	Age[1b]	Region[2]	Surrounding crustal thickness (km)[3]	Crustal thickness ratio[3]
Freundlich-Sharonov[a]	175°E, 18.3°N	582	PN8 (PN/N)	FHT-An	45.3 ± 0.2	0.27 ± 0.001
Moscoviense[a]	149°E, 27.5°N	629	N1 (N)	FHT-An	39.0 ± 0.7	0.16 ± 0.003
Mendel-Rydberg[a]	93.7°W, 50.0°S	636	N1 (N/PN)	FHT-O	33.6 ± 0.9	0.34 ± 0.01
Nectaris[a]	34.7°E, 14.5°S	915	N1 (N)	FHT-O	29.4 ± 1.9	0.25 ± 0.02
Hertzsprung[a]	129°W, 2.02°N	549	N2 (N/PN)	FHT-An	50.1 ± 0.7	0.38 ± 0.01
Humboldtianum[a]	82.0°E, 57.2°N	603	N2 (N)	FHT-O	30.2 ± 0.3	0.15 ± 0.001
Serenitatis[a]	18.9°E, 27.0°N	659	N2 (PN?)	PKT	28.2 ± 1.0	0.25 ± 0.01
Serenitatis[b]	18°E, 26°N	920	N2 (PN?)	PKT	27.0 ± 0.8	0.25 ± 0.00
Humorum[b]	39.5°W, 24°S	820	N2 (N)	PKT	32.0 ± 1.0	0.24 ± 0.01
Crisium[a]	59.8°E, 17.0°N	1092	N2 (N)	FHT-O	29.9 ± 2.5	0.07 ± 0.01
Orientale[a]	94.6°W, 19.7°S	928	I (I)	FHT-O	38.2 ± 1.7	0.20 ± 0.01
Imbrium[a]	17.4°W, 33.5°N	1114	I (I)	PKT	29.2 ± 1.1	0.36 ± 0.01

[1] PN, N, and I indicate Pre-Nectarian, Nectarian, and Imbrian, respectively. Ages in parentheses are revised estimates based on LRO data (Fassett et al., 2012).

[2] PKT, FHT, and SPAT indicate the Procellarum KREEP Terrane, the Feldspathic Highlands Terrane (An, the central anorthositic region; O, the outer region), and the South Pole-Aitken Terrane, respectively (Jolliff et al., 2000).

[3] A GRAIL crustal thickness model (34 km on average) is used.

[a] Head et al. (2010)

[b] Wilhelms (1987)

Table 2: Parameter values adopted for the nominal case. Most thermal parameters are taken from Mohit & Phillips (2006).

Symbol	Quantity	Value	Unit
R_p	The radius of the Moon	1737	km
$R_{\rm lm}$	The radius of the lower mantle	1637	km
$R_{\rm co}$	The radius of the core	300	km
$D_{\rm cr}$	Crustal thickness	20–60	km
$\rho_{\rm cr}$	Crustal density	2550	kg m^{-3}
$\rho_{\rm um}$	Upper mantle density	3220	kg m^{-3}
$\rho_{\rm lm}$	Lower mantle density	3400	kg m^{-3}
$\rho_{\rm co}$	Core density	6000	kg m^{-3}
T_s	Temperature at the surface	250	K
$T_{\rm CMB}$	Temperature at the core-mantle boundary	1700	K
$k_{\rm cr}$	Crustal thermal conductivity	1.5	W m^{-1} K^{-1}
$k_{\rm ma}$	Mantle thermal conductivity	3.0	W m^{-1} K^{-1}
C_p	Specific heat	1200	J kg^{-1} K^{-1}
L	Latent heat of fusion of the mantle	6.75×10^5	J kg^{-1}
μ	Shear modulus of silicate	50	GPa

Table 3: Rheological parameters adopted. Values for dry anorthite (Rybacki & Dresen, 2000) and those for dry peridotite (Lawlis, 1998) are used for the crust and mantle, respectively.

Symbol	Crustal value	Mantle value	Unit
A	$10^{12.7}$	$10^{7.6}$	MPa^{-n} s^{-1}
E^*	648	600	kJ mol^{-1}
n	3	3.5	Dimensionless

Table 4: Constraints on the formation ages of early Pre-Nectarian basins following solidification of the LMO. The unit is Myr. For a deep LMO case, $t = 0$ assumes the time after mantle overturn. Later formation ages are allowed for a deep LMO case because large-scale mantle overturn significantly heats the Moho.

Mean crustal thickness	Deep LMO	Shallow LMO
34 km	$t_{\mathrm{form}} < 50$	$t_{\mathrm{form}} < 0$
43 km	$0 < t_{\mathrm{form}} < 150$	$t_{\mathrm{form}} < 50$